Los Alamos NATIONAL LABORATORY EST.1943

LA-UR-14-29206 (Accepted Manuscript)

Investigation of Structural Heterogeneity at the SPE Site Using Combined P-Wave Travel Times and Rg Phase Velocities

Rowe, Charlotte Anne
Patton, Howard John

Provided by the author(s) and the Los Alamos National Laboratory (2016-08-29).

To be published in: Bulletin of the Seismological Society of America

DOI to publisher's version: 10.1785/0120150022

Permalink to record: http://permalink.lanl.gov/object/view?what=info:lanl-repo/lareport/LA-UR-14-29206

Disclaimer:
Approved for public release. Los Alamos National Laboratory, an affirmative action/equal opportunity employer, is operated by the Los Alamos National Security, LLC for the National Nuclear Security Administration of the U.S. Department of Energy under contract DE-AC52-06NA25396. Los Alamos National Laboratory strongly supports academic freedom and a researcher's right to publish; as an institution, however, the Laboratory does not endorse the viewpoint of a publication or guarantee its technical correctness.

RESEARCH LIBRARY

Bulletin of the Seismological Society of America, Vol. 105, No. 5, pp. 2379–2389, October 2015, doi: 10.1785/0120150022

Investigation of Structural Heterogeneity at the SPE Site Using Combined *P*-Wave Travel Times and *Rg* Phase Velocities

by Charlotte A. Rowe and Howard J. Patton

Abstract We present analyses of the 2D seismic structure beneath Source Physics Experiments (SPE) geophone lines that extended radially at 100 m spacing from 100 to 2000 m from the source borehole. With seismic sources at only one end of the geophone lines, standard refraction profiling methods cannot resolve seismic velocity structures unambiguously. In previous work, we demonstrated overall agreement between body-wave refraction modeling and *Rg* dispersion curves for the least complex of the five lines. A more detailed inspection supports a 2D reinterpretation of the structure. We obtained *Rg* phase velocity measurements in both the time and frequency domains, then used iterative adjustment of the initial 1D body-wave model to predict *Rg* dispersion curves to fit the observed values. Our method applied to the most topographically severe of the geophone lines is supplemented with a 2D ray-tracing approach, whose application to *P*-wave arrivals supports the *Rg* analysis. In addition, midline sources will allow us to refine our characterization in future work.

Introduction

The Source Physics Experiment (SPE) is a series of chemical explosions being conducted via the U.S. Department of Energy's National Nuclear Security Administration (Snelson *et al.*, 2013). The purpose of the SPE is to develop a physics-based, comprehensive and broadly applicable model of the explosion source. By improving our understanding of the explosion source, in particular how observed phenomena (such as shear waves) are generated, we will augment our technical capabilities for monitoring underground nuclear tests worldwide.

The experiments and data collection systems target a variety of phenomena, but this article focuses on the development of preliminary, data-driven seismic velocity models for the experiment site. Without a reliable seismic model, the far-field observations, which are generally all we have for foreign nuclear explosions, cannot be confidently related to the near-field source phenomena.

In addition to close-in accelerometer deployments and near-regional distance broadband seismometers (Townsend and Mercadante, 2014), a network of five linear geophone spreads was installed, which extend at 100 m intervals to distances of 2 km radially from the shot hole in this first phase of the project. Figure 1 shows not only the geophone lines but also the topography of the experiment site and known major faults. The Phase I SPE site was selected for presumed simple, uniform structure on a massive granitic batholith (Climax Stock) to provide an experimental setting analogous to hard-rock nuclear test sites such as Semipalatinsk in central Asia and Pyunggye-ri in North Korea. Later, Phase II is planned for a soft-rock location. It has been amply demonstrated through the course of the experiment to date that the geology of the Phase I site is not simple, but is rather, quite complex, providing a challenge for seismologists analyzing the data and developing the velocity models to be applied in other studies, such as moment tensor modeling.

Data

The five-spoked arrangement of geophone lines that extend from 100 m to 1.9 km (Fig. 1) consists of Geospace GS-11D 4.5 Hz sensors, a majority of which are only vertical components, but the 4th, 8th, 12th and 16th sensors from the shot point on each line are three component, with horizontal components nominally oriented in radial and tangential directions. Data were recorded at 2 ms sample rate on 6-channel RefTek 130 digitizers. The digitizers were powered by batteries trickle charged by solar panels. Data were stored to disk and collected manually at intervals. Because geophones produce negative voltages for upward ground motion, unlike seismometers, the first motions for the compressional arrivals are downward (Fig. 2). Geophones were buried at depths less than 0.5 m in native material, with sandbags placed on top (Townsend and Mercadante, 2014). After April 2014, the single-component geophones were switched to three component and most data are now telemetered to the University of Nevada Reno (UNR) Nevada Seismological Laboratory (NSL).

Waveform data were converted to the RefTek raw format and then converted to miniSEED format at the NSL. All logs and raw- and miniSEED-formatted files were then mirrored to a second disk array for distribution to project investigators

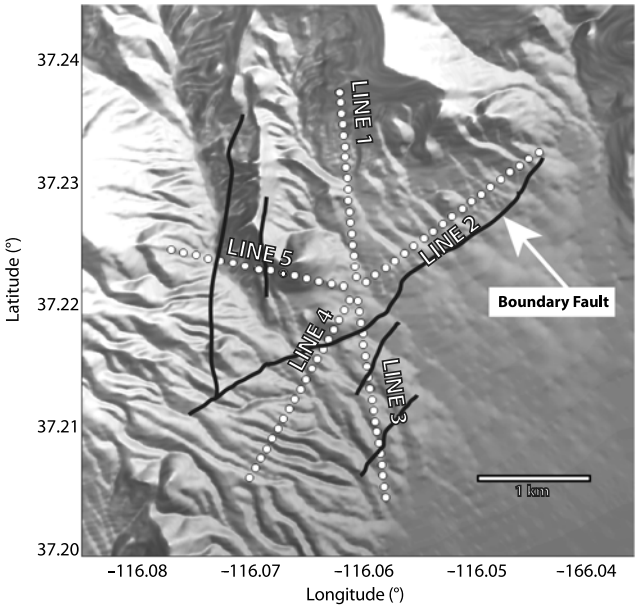

Figure 1. Source Physics Experiments (SPE) site showing topography, five geophone lines (white circles) and known major faults (black lines) whose traces cross the geophone lines and which impact the velocity profiles presented in this study.

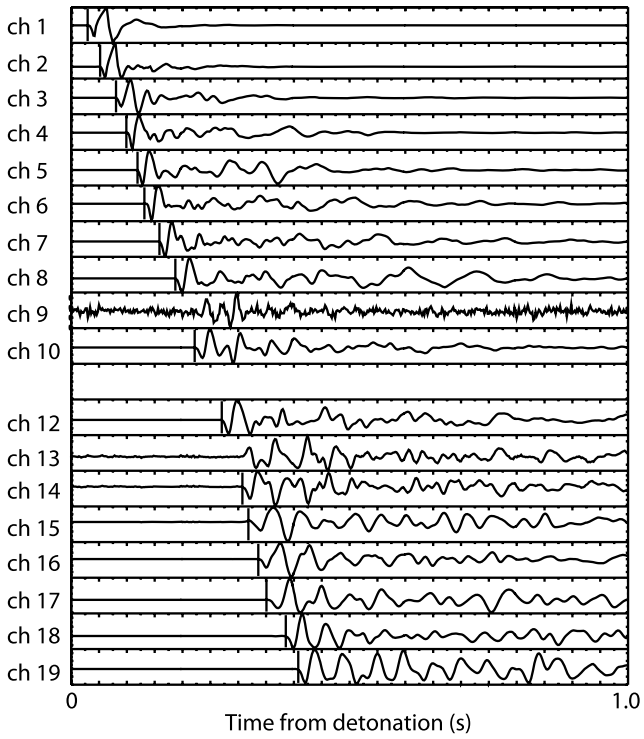

Figure 2. Waveforms for first arrivals at geophones on line 2 for the second of the experiment shots (SPE-2). Channel 11 is missing and channels 9 and 13 exhibit cross-talk problems. One second of data is shown.

(Townsend and Mercadante, 2014). Following download from NSL, we converted these to Seismic Analysis Code (SAC) for our analysis. The three shots (SPE-1, SPE-2, and SPE-3) whose data were available for this analysis are detailed in Table 1, parameters from Mellors *et al.* (2012).

To date, three of the seven planned shots have been detonated successfully. Seismic data from these shots are currently being leveraged for improved modeling of the sources, but models of the wave propagation at the site are needed to allow for interpretation of the source. We take a two-pronged approach to develop the 2D seismic profiles along the five geophone lines, which includes both refraction interpretation based on first-arriving *P* waves and also velocity profiling based on fitting fundamental-mode Rayleigh-wave (*Rg*) phase velocity curves obtained from both time-domain and frequency-domain measurements. Augmenting refraction analysis with short-period *Rg* dispersion measurements is not a new approach, although methodologies may differ in detail. Astrom and Lund (1994) used short-period *Rg* to determine shear velocities in the uppermost part of the crystalline Baltic shield in southern Sweden, resulting in inferred *P*-wave models. We will determine a preliminary *P*-wave model based on our first-arrival detections for the geophone lines. Then we will obtain a fundamental-mode *Rg* dispersion curve for these lines, whose form will be reconciled with the body-wave models permitted through our *P*-wave analysis.

P-Wave Refraction Analysis

We begin our analysis by examining the data for line 2, which runs N50°E from the borehole, exhibits the smallest topographic variation, and crosses no major exposed faults (Fig. 1). In Figure 2, we show waveforms recorded on line 2 for the second shot, SPE-2, which was much larger than SPE-1 and provides superior signal-to-noise ratio for first-arrival analysis. After correcting some data and channel quality issues, we were able to identify first-arriving energy for each of the working sensors. In our initial body-wave analysis, we treat the problem as a simplified seismic refraction experiment.

The technique for obtaining a simple, 1D velocity model from active source profiles is summarized in Dobrin (1952). Assuming the simplest possible model, the one-shot/many-receivers linear seismic profile is initially characterized by planar, parallel, homogeneous, isotropic, flat-lying horizons of increasing velocity with depth, whose *P*-wave velocities and depth to interfaces can be ascertained with the application of Snell's law. For a hypothetical (simplest) structure, with an overburden having velocity V_0 and basement beneath it of contrasting $V_1 > V_0$ the direct seismic ray emanating from the source expands as a spherical wavefront, but can be thought of as a ray traveling along the geophone spread at a velocity of V_0 (Fig. 3). The critically refracted head wave first appears at the critical refraction distance as a reflected phase, and propagates along the interface between overburden and bedrock at a velocity of V_1, constantly sending up critically refracted wavefronts along the sensor

Table 1
Source Physics Experiments (SPE)-1, SPE-2, and SPE-3 Explosion Parameters

Shot Number	Date (yyyy/mm/dd)	Time (GMT) (hh:mm:ss.sss)	Depth (m)	Yield (eq. TNT) (kg)
SPE-1	2011/05/03	22:00:00.011	55	87.9
SPE-2	2011/10/25	19:00:00.012	45.7	997
SPE-3	2012/07/24	18:00:00.448	45.8	905

Three shots executed prior to this analysis. Dates, times, shot depths, and yields are indicated for each (Snelson *et al.*, 2013). GMT, Greenwich mean time; TNT, trinitrotoluene.

line. At the crossover distance, it overtakes the direct wave and provides the first-arriving energy thereafter.

By implementing these simplified assumptions, we estimate a 1D model for line 2. Arrival times are plotted as a function of lateral distance for the reliable channels on line 2 for shot SPE-2 in Figure 4. Graphical analysis of Figure 4 provides us with an apparent velocity of 4.76 km/s for the first interface, and 6.2 km/s for a second, deeper interface. The failure of the 4.76 km/s regression line to pass through the origin is partly due to the shot depth (45 m for SPE-2), which accounts for less than 0.01 s of the offset. The remaining offset suggests the existence of a thin, slower, uppermost layer, which we are unable to constrain with confidence because the first geophone, at a distance of 100 m from the shot, is at or beyond the crossover distance (Fig. 3). We estimate a maximum possible velocity for V_0 assuming a zero-depth source, and a maximum possible thickness Z_0 for this topmost layer.

Using the crossover distance between line fits for V_0 and V_1 first-layer crossover-based thickness Z_c:

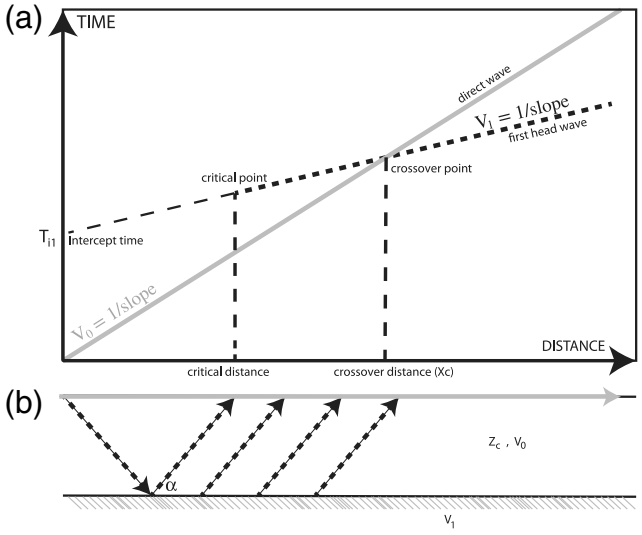

Figure 3. Hypothetical, idealized seismic refraction profile analysis. (a) Anticipated first-arrival time (y axis) as a function of distance along the spread (x axis). V_0 and V_1 can be determined from the inverse slopes of their associated T/X linear fits. Depth to the interface, Z_0, is calculated by finding the crossover distance, X_c (in which the refracted arrivals overtake the direct) and using equation (3). (b) Seismic wavefront can be visualized as a direct ray (solid gray) and refracted rays (dashed black) propagating at V_0 and V_1, respectively.

$$Z_c = \frac{x_c}{2}\sqrt{\left[\frac{V_1 - V_0}{V_1 + V_0}\right]} = 32 \text{ m}. \quad (1)$$

Using the time intercept of V_1 line, the intercept-based thickness Z_i is

$$Z_i = \frac{T_{i1}}{2}\left[\frac{V_1 V_0}{\sqrt{V_1^2 - V_0^2}}\right] = 31 \text{ m}, \quad (2)$$

in which T_{i1} refers to the time intercept for the refracting horizon exhibiting velocity V_1. Both yield apparent depths to the interface that are in good agreement. Using the time intercept for the V_2 line (6.2 km/s) fit, with the Z_0 determined above and the three velocities determined through graphical line fitting, we can estimate depth to the second interface:

$$Z_1 = \frac{1}{2}\left[T_{i1} - 2Z_0\frac{\sqrt{V_2^2 - V_0^2}}{V_2 V_0}\right]\frac{V_2 V_1}{\sqrt{V_2^2 - V_0^2}} = 520 \text{ m}. \quad (3)$$

Thus, we have a preliminary 1D velocity model for line 2 as outlined in Table 2.

Recalling our preliminary assumptions that allowed us to derive this model, we are not convinced of either the depths to interfaces or the estimated velocities, based on first-arrival analysis alone. In seismic refraction profiling, equations (1)–(3) are applicable only in the case of layer-cake-type geology with planar, flat-lying horizons separating distinct homogeneous strata exhibiting increasing velocity with depth. With a seismic source at only one end of the geophone spread(s), it is impossible to resolve even a first-order complication, that is, a dip angle for one or both detected horizons. The 4.76 and 6.2 km/s horizons interpreted from line 2 can be regarded only as apparent velocities, and the depths to the interfaces are only apparent depths. Figure 5 illustrates the problem, as well as the first-order solution, which is to provide a seismic source at the far end of the geophone line, or reverse the profile.

For the case sketched in Figure 5, the shallowest layer velocity V_0 is accurately determined from either end, because the direct wave is affected only by the (assumed homogeneous) uppermost layer. We can use the apparent velocities V_{1u} updip and V_{1d} downdip, to find the dip angle α, and true V_1:

$$\alpha = \frac{1}{2}(\sin^{-1} V_0 m_d - \sin^{-1} V_0 m_u) \quad (4)$$

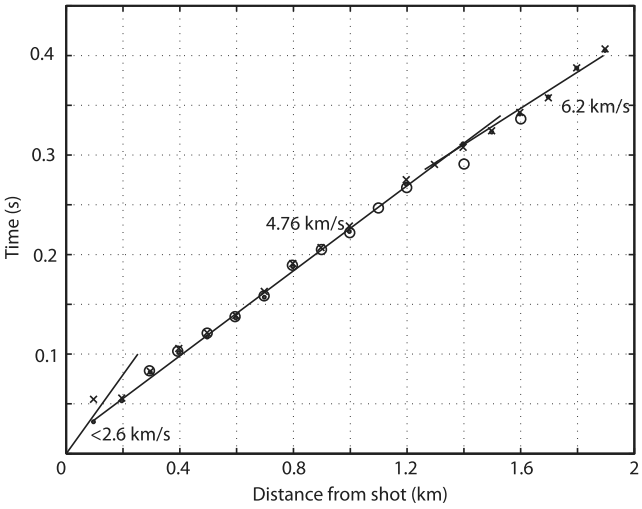

Figure 4. Line 2 time–distance plot showing *P*-wave arrivals for SPE-1 (circles), SPE-2 (dots), and SPE-3 (crosses). Apparent direct wave and refracted wave velocities estimated assuming a flat-lying structure. The bulk of the arrivals describe a horizon whose apparent velocity is 4.76 km/s, underlain by a deeper layer with an apparent velocity of ~6.2 km/s. The shallowest material is too thin and too slow for a crossover distance to be established. We can only assume this is less than or equal to the value given by the arrival and offset of the first receiver.

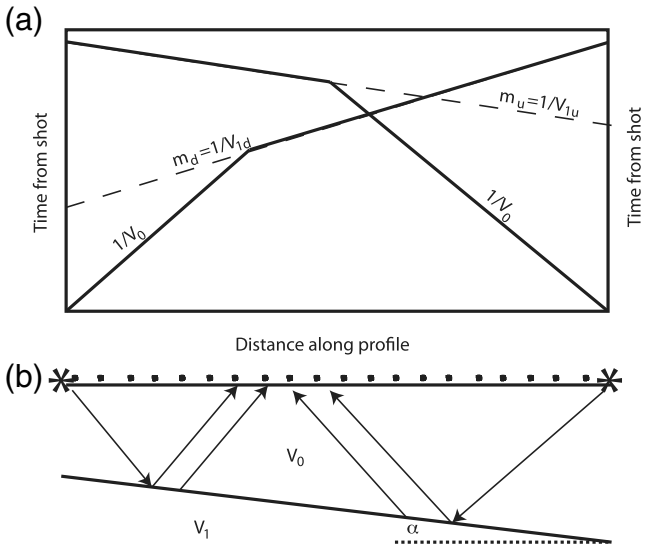

Figure 5. (a) Idealized first-arrival refraction analysis for (b) a dipping layer over a half-space. Shots at each end are indicated by asterisks, and receivers are black squares. Although V_0 (velocity of the direct arrival) is consistent for both directions, the arrivals for the dipping V_1 layer provide different apparent velocities updip (V_u) and downdip (V_d). Reversing the profile allows resolution of the structure, whereas with a source at only one end or the other will yield misleading results. See equations (4) and (5).

and

$$V_1 = \left(\frac{2V_{1u}V_{1d}}{V_{1u} + V_{1d}}\right)\cos\alpha, \tag{5}$$

in which m_d and m_u are the slopes of the downdip and updip refracted phase as a function of distance, respectively (Fig. 5), and V_{1u} and V_{1d} are their reciprocals. Neither V_1 nor α can be determined from an individual geophone line from one off-end shot; however, some approximations derived from treating pairs of profiles as split spreads are discussed below.

Rg Phase Velocity Studies

The SPE shots provide us with well-recorded high-frequency Rayleigh (*Rg*) waves, which can serve to reduce uncertainty in the model derived from the first arrivals, and provide an alternate and independent validation of the shallow seismic wavespeeds. Body-wave and surface-wave analyses have long been used jointly (e.g., Julià *et al.*, 2000; Lawrence and Wiens, 2004) to constrain seismological structure, and improve the derived model over that from one parameter alone.

Table 2
Preliminary 1D Model for Line 2

Depth to Layer (m)	V_P (km/s)
0	2.6–3.0
~32	4.76
~520	6.2

The use of *Rg* phase velocity dispersion provides a significant advantage over refraction analysis, in that the *Rg* is sensitive to even very thin (hidden) layers, as well as to velocity inversions, whereas these features may be invisible in a simple refraction analysis. Our particular concern, due to geophone spacing and shot, is the inability to resolve the shallowest part of the model. Our *Rg* fundamental phase dispersion measurements are performed both in the time domain, via narrowband filtering of the waveforms and manual identification of consistent phase peaks, and also in the frequency domain, via Fourier transform, unwrapping of the continuous phase function for each geophone, and linear inversion for propagation velocity at selected frequencies.

Time-Domain Analysis

The most intuitive and straightforward approach to building an *Rg* phase dispersion curve is narrowband filtering of the shot gather, and visual determination of the moveout for a selected peak, trough or zero crossing in the filtered time series (traces) for each frequency band. Plotting the arrivals as a function of geophone distances allows fitting a line whose inverse slope is the phase velocity at the selected frequency. This can be done in a suite of frequency bands, building a phase propagation function for the geophone line.

Figure 6 illustrates selected narrowband filtered realizations of the line 2 waveforms, with phase moveout indicated. We note that the phase velocity appears to vary along the length of the line, indicating that a 1D model may be inappropriate for this, simplest, profile. In this example, we can

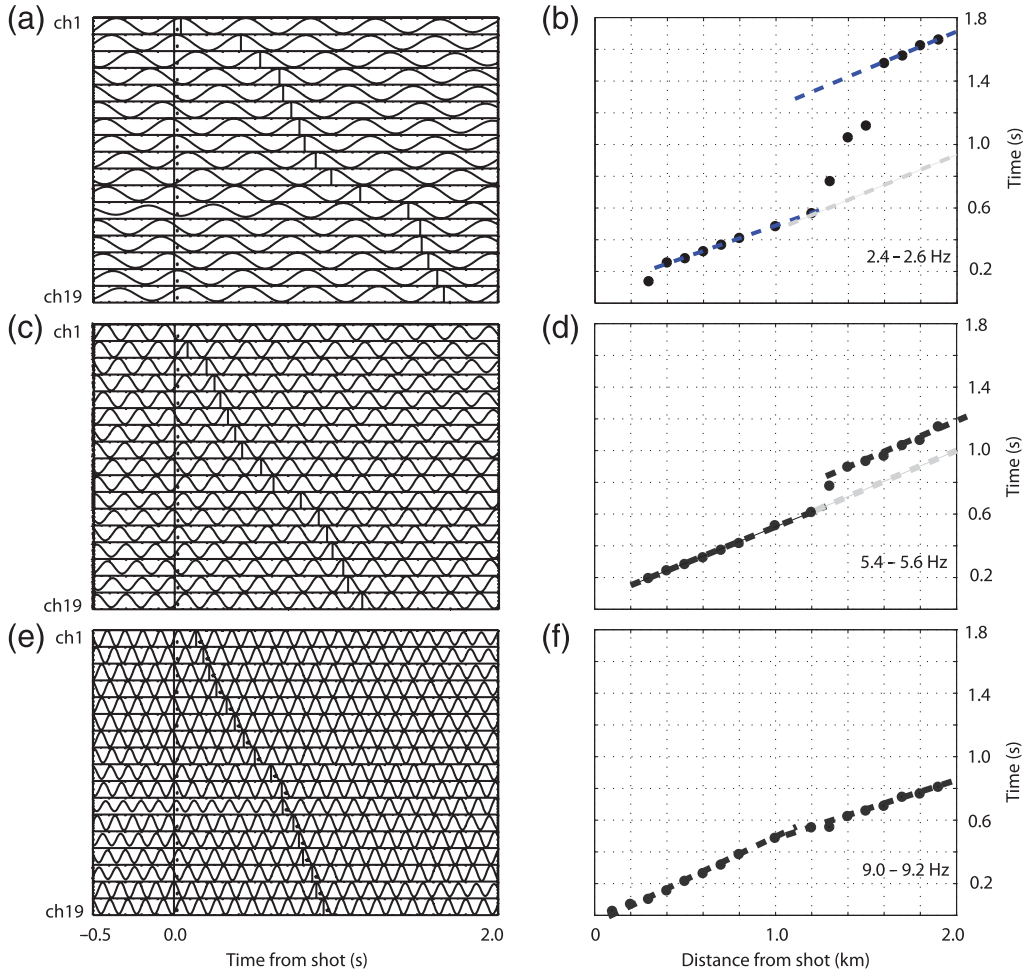

Figure 6. Line 2 examples of time domain *Rg* phase velocity analysis. (a) Narrowband filtered traces between 2.4 and 2.6 Hz, with phase moveout for *Rg*. Channels 9 and 11 are missing. (b) Phase picks as a function of distance at 2.4–2.6 Hz. Dotted black lines indicate best-fit line where possible. Inverse slope of this line provides the fundamental phase velocity at this frequency. The gray dotted line shows distal slope, carried downward to illustrate comparison of velocity before, and after, *Rg* disruption midline. (c) Same as (a), but for 5.4–5.6 Hz. (d) Same as (b), but for 5.4–5.6 Hz. (e) Same as (a) and (c), but for 9.0–9.2 Hz. (f) Same as (b) and (d) but for 9.0–9.2 Hz. Different behaviors indicate that the dispersion curve, and therefore velocity function, differs from proximal to distal portions of the line.

see a significant disruption midline, particularly evident in the lower frequencies, which naturally would require more lateral distance to re-establish a coherent wavetrain following a structural or material heterogeneity. The re-established *Rg* propagation beyond about 1500 m exhibits a slightly different phase velocity than the proximal region of the line. Higher frequencies exhibit a pronounced velocity change between the proximal and distal segments of this line, consistent with a generally anticipated greater variation in shallow material properties. We have opted to divide the model into proximal and distal segments for the geophone lines, producing approximate 1D models for each segment, which is the best detail we can achieve given the limited spatial sampling at this time. We show the frequency-dependent phase velocity functions for proximal (ch3–ch8) and distal (ch11–ch19) in Figure 7. Proximal behavior is more consistent than distal, but inspection of the two functions indicates that the velocity profiles for the two segments are somewhat different. Above 10 Hz, the values are likely contaminated by *P*-wave energy (e.g., Rodgers *et al.*, 2010), and we will not include these higher wavespeeds at higher frequencies in our efforts to fit a dispersion curve for fundamental-mode *Rg*.

Frequency-Domain Analysis

An alternative approach to the time-domain analysis above is computing the phase velocity in the frequency domain. This is similar to the spectral analysis of surface waves (SASW) approach pioneered by Heisey *et al.* (1982) and widely used in geotechnical applications, such as pavement profiling (Ryden, 2004). The SASW method was expanded to the multichannel analysis of surface waves. These methods assume plane surface-wave propagation between the receivers and a smooth continuous dispersion curve that can be found via the unwrapped phase spectra (Al-Hunaidi, 1992). Surface-wave frequency components need to propagate some distance from the source before a plane wave can

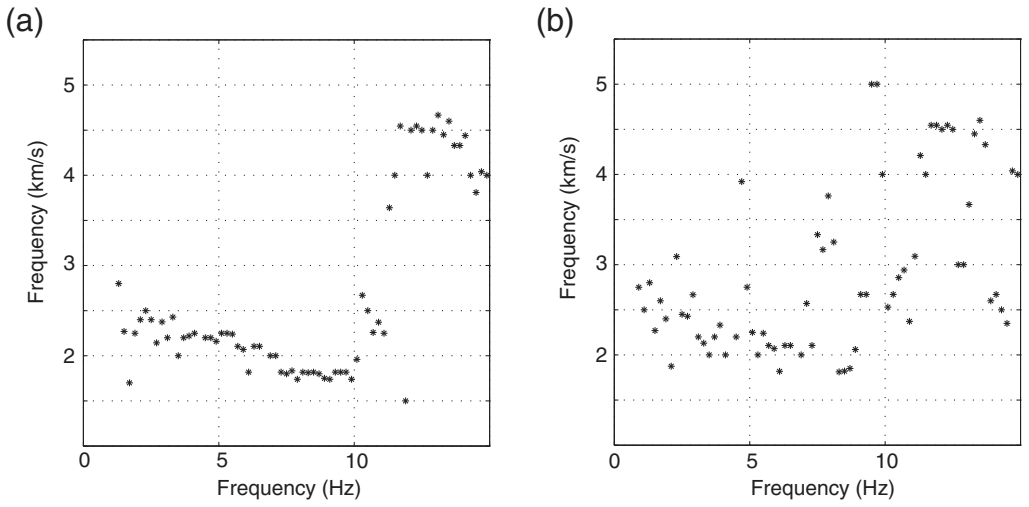

Figure 7. Line 2 *Rg* phase velocities manually determined in time-domain analysis. (a) Proximal geophones (ch3–ch8). (b) Distal geophones (ch11–ch19). Proximal values are more consistent than distal, but distal values do suggest a slightly different velocity profile. Values above 10 Hz are considered to be contaminated with *P*-wave energy.

be assumed (Ganji *et al.*, 1998). This near-field effect generally extends about one half-wavelength from the source (Stokoe *et al.*, 1994), so is more problematic for longer-period measurements. There is also a far-field effect in which high-frequency surface waves are contaminated by body waves (Park *et al.*, 1999). Our approach is analogous to the SASW method, but applied to a series of detectors in a line. In this approach, we perform a discrete Fourier transform on the waveforms for the selected geophone line and then unwrap the phase spectrum for each channel. Figure 8 shows the unwrapped phase functions for the proximal section of line 2. We seek the relative phase shift $\Delta\phi$ between each channel at any selected frequency, f. To find the phase velocity C, which we will characterize as the slowness, $S = 1/C$:

$$\frac{\Delta\phi(f)}{f} = D \times S(f), \tag{6}$$

in which D is the distance along the line. For data represented as $\Delta\phi(f)/(f)$ (equation 6) as a function of D across several channels, we find the slowness S by performing a linear regression of values at each selected frequency, f (Fig. 9). The proximal and distal frequency-dependent phase velocity measurements for line 2 are illustrated in Figure 10, demonstrating rough agreement between the time-domain and frequency-domain approaches between about 3 and 10 Hz. It is clear that the time-domain analysis

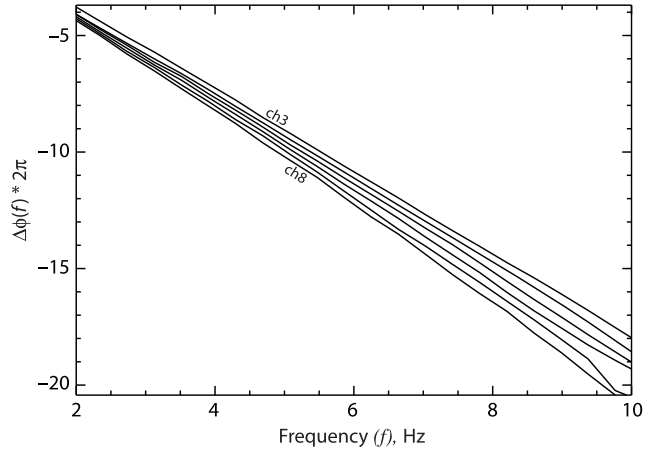

Figure 8. Unwrapped phase functions for channels 3–8, line 2. Increasing distance from the shot (ch8) exhibits a steeper phase slope as a function of frequency. Functions would ideally converge at the 0, 0 intercept, but the near stations are not coherent at lower frequencies due to the near-source effect. This can be observed in the divergence at lower frequencies for channel 3, which is well behaved beyond 3 Hz and up to roughly 10 Hz.

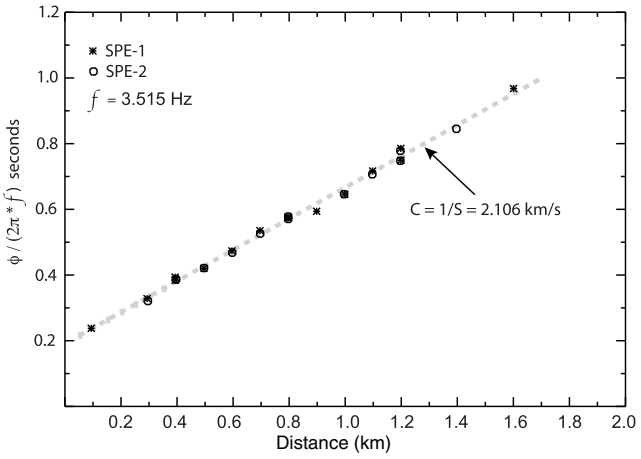

Figure 9. *Rg* phase velocity at a frequency of 3.515 Hz for line 2. Data for SPE-1 and SPE-2 combined, asterisks represent measurements from SPE-1 waveforms and circles are readings from SPE-2. Phase velocity is the inverse of the slope of the least-squares regression (gray dotted line).

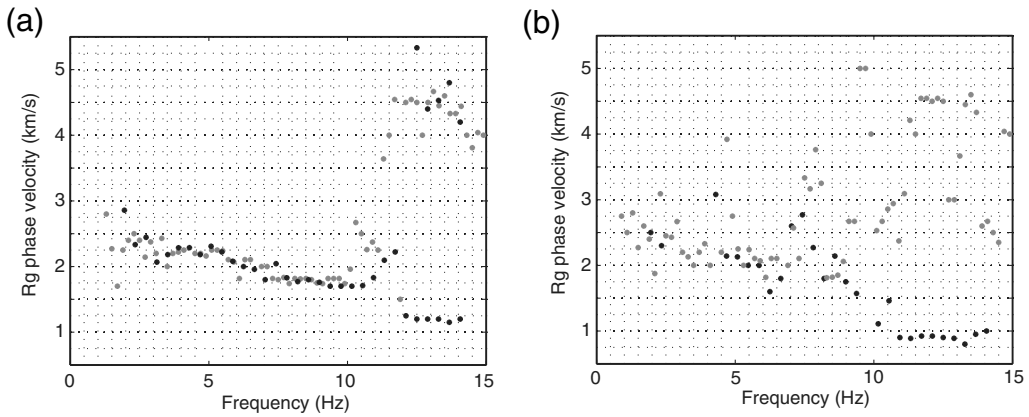

Figure 10. Time-domain (gray) and frequency-domain (black) measurements for *Rg* on the (a) proximal and (b) distal segments of line 2. Proximal results appear well organized and consistent between the two methods from 3 to 10 Hz, whereas considerably more scatter is evident in the distal segment.

was subject to *P*-wave interference at the higher frequencies, as evidenced by >4 km/s values exhibited on the proximal segment above 10 Hz. Distal measurements are more scattered for both methods, but a coherent curve is evidenced in the frequency domain, whereas time-domain readings lose coherency above ~7 Hz.

Discussion

We construct velocity models for the SPE Phase I site that are consistent with *Rg* phase velocity and *P*-wave refraction observations. These models will be used by other researchers addressing issues of the explosion source and its effect on far-field seismic propagation to appropriately develop their predictive capabilities and compare them with the observed waveforms.

We applied the forward-modeling code, MODESB (Schwab *et al.*, 1984), to predict *Rg* dispersion for a given body-wave velocity model. This FORTRAN-77 software, developed at Lawrence Livermore National Laboratory by K. Nakanishi, accepts as input a 1D layered model specifying *P* and *S* wavespeeds and material density, ρ. The range of frequencies for which to compute dispersion is also specified. The code generates theoretical fundamental- and higher-mode *Rg* dispersion curves. We focus on the fundamental mode in our study, recognizing that higher modes may play a role in the scatter observed among the higher-frequency measurements. Iterative adjustments to the input model, which are derived from the first-arrival refraction analysis, allow us to obtain a theoretical dispersion curve that qualitatively fits the *Rg* measurements.

Because we have determined by inspection that the structure or material properties for line 2 can easily be divided into proximal and distal sections, we anticipate that our final results may yield two different 1D body-wave models that produce the best fit to our *Rg* observations. Although the single off-end explosion source does not allow us to determine unequivocally whether line 2 can be characterized by flat horizons, we note the geometry of the five radial geophone lines allows us to consider the treatment of some pairs as approximate split-spread configurations (Fig. 1). Lines 1 and 3, for instance, are almost collinear. Lines 2 and 4, although at a moderate angle, appear to be the reasonable candidates for a first-order examination as split-spread segments, largely to validate the assumption of an apparent versus true velocity for the first-refracted layer (leaving aside its depth). Figure 11 shows the first breaks for lines 2 and 4, plotted as if they were collinear in a split spread. We observe that neither line allows true constraint of the shallowest layer, but both exhibit a refracting horizon in their proximal segments with similar, but distinct, *P*-wave velocities (4.76 and 4.5 km/s for lines 2 and 4, respectively). Using equations (4) and (5), we estimate a dip angle for this horizon and true velocity, which are $\alpha = 1.4°$ toward the eastern (distal) end of line 2 and $V_1 = 4.625$ km/s.

We next invoked the MODESB program, providing as a starting body-wave model the simple 1D model that was initially derived for the full length of line 2 (Table 2). Predicted *Rg* curve fit was poor, so we began adjusting the model iteratively, both in terms of wavespeed and layer thicknesses. The deeper horizon of ~6.2 km/s is not well constrained in the refraction data so we did not adjust this velocity, although the interface had to be deepened to improve the fit for the distal *Rg* measurements. To better fit the middle-to-high *Rg* frequency measurements, we needed to decrease the body-wave velocities considerably for the weathered horizon and divide it into three layers. Figure 12 shows the final theoretical *Rg* curves, produced by the body-wave models presented in Table 3. V_P/V_S was held constant at 1.73 for the modeling, and values of material density were approximated from well-log information (Townsend and Mercadante, 2014). We note that the final *Rg* models imply a depth to the 4.6 km/s interface that differs for each half of line 2, consistent with the dip direction estimated from the split-spread approximation for lines 2 and 4. The dip angle is approximately 0.6°, roughly half of that estimated from the

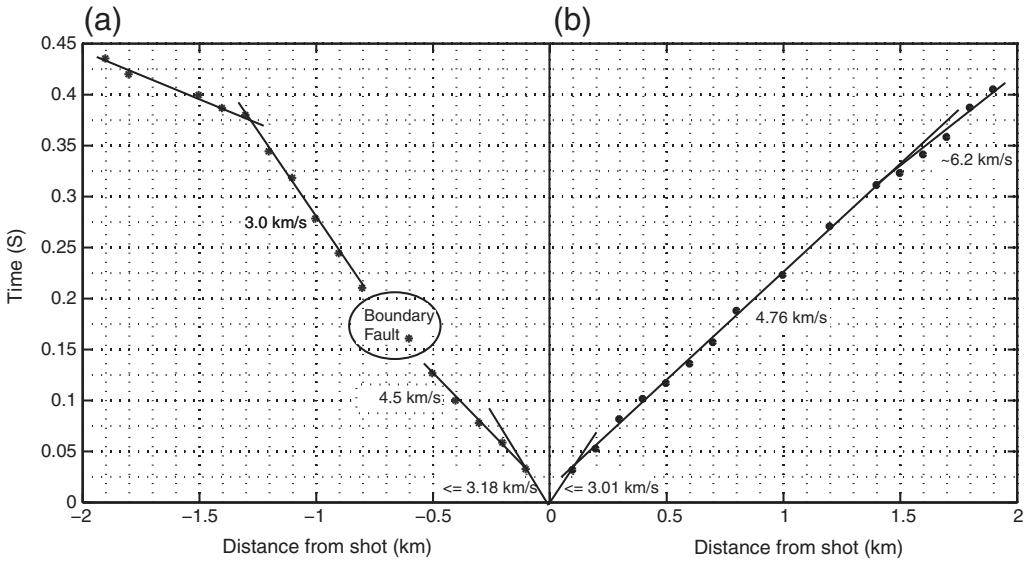

Figure 11. First arrivals for (a) line 4 and (b) line 2 plotted as a split spread. Note the disruption on line 4 where the Boundary fault is crossed by the geophone line, with slower, 3.0 km/s material beyond (south) of the fault. This is consistent with the 245 m throw (Townsend *et al.*, 2012) of this fault providing a thick stack of sediments over the bedrock to the southeast. Shallowest layer ~3 km/s near the source is unconstrained for both sections, but the fairly robust 4.76 km/s refractor on line 2 appears on line 4 with an apparent velocity of 4.5 km/s, until it is disrupted by the fault.

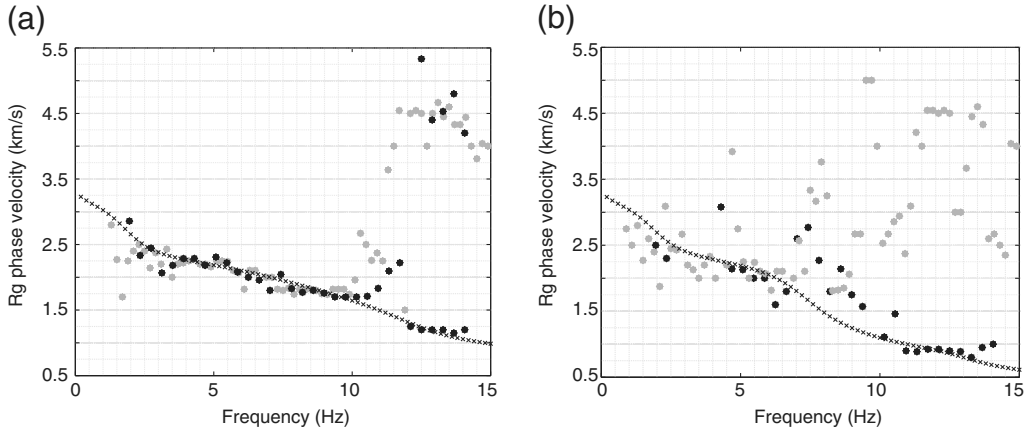

Figure 12. Final predicted dispersion curves for (a) proximal and (b) distal segments of line 2. Gray dots, time-domain phase measurements; black dots, frequency-domain phase measurements; small crosses, predicted *Rg* fundamental-mode phase velocity function for body-wave models detailed in Table 3.

Table 3
Final Models for Line 2

Proximal Depth to Interface (m)	V_P Proximal	V_S Proximal	Distal Depth to Interface (m)	V_P Distal	V_S Distal
4	0.85	0.49	7.5	0.75	0.43
8	0.95	0.55	15	0.95	0.55
36	2.0	1.16	26	2.0	1.16
516	4.6	2.66	496	4.6	2.66
Inf	6.2	3.58	Inf	6.2	3.58

1D body-wave models for proximal and distal segments of line 2. We used a constant V_P/V_S of 1.73 in the modeling with values of density consistent with values derived from well logs (Townsend and Mercadante, 2014).

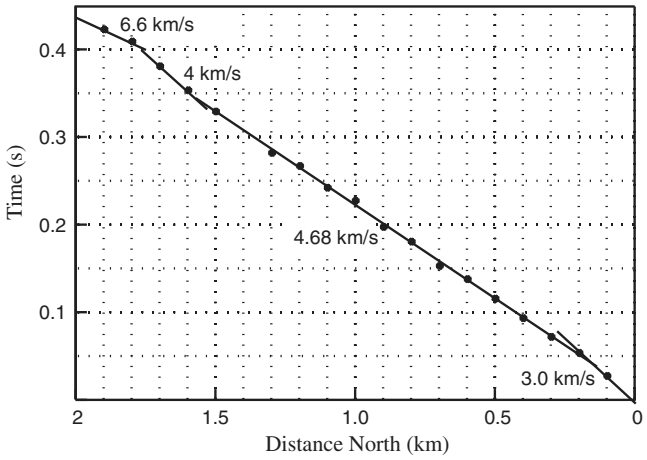

Figure 13. *P*-wave time–distance plot for line 1 arrivals, SPE-2. Notice apparent velocity reversal from about 1300 to 1700 m, from 4.68 to ~4 km/s. Near-source velocity of ≤3 km/s is consistent with other analyzed lines.

split spread. This discrepancy reflects the poor constraint on our model as a result of limited sampling and the coarse experimental design.

We applied our body-wave and surface-wave analyses also to line 1, whose exaggerated topography provides challenges from a variety of perspectives. *P*-wave arrivals provide the time–distance plot in Figure 13 that exhibits what appears to be a velocity reduction from ~4.6 to ~4.0 km/s between 1300 and 1700 m from the shot. The MODESB analysis applied to the proximal (100–1000 m) and distal (1100–1900 m) segments of the line (Fig. 14) provide 1D body-wave velocity models for each section, after fitting the *Rg* phase measurements made in both time domain and frequency domain. These body-wave models are presented in Table 4. We observe a considerable thickening of the shallow, slow material in the distal portion of the line. In an alternate approach for line 1, we used a 2D ray-tracing code, RAYINVR (Zelt and Smith, 1992), to examine *P*-wave velocity variations along this line. With only one shot location, the structure is inadequately constrained to perform a meaningful inversion with freely varying horizons as well as freely varying velocities. Lacking any additional information, a topographically compliant surface featuring a thin weathering layer over country rock provides a reasonable starting model, thus we applied the line 2 proximal 1D model, draping it over the topography. We hold these horizons fixed and allow the velocity to vary. The resulting cross-section velocity profile reduces root mean square travel-time misfit from 0.02 to 0.011 s, or by 45%. Resulting velocity contours are shown in Figure 15. We freely acknowledge that this approach is coarse and tells us little more than the MODESB analysis did, which is that the material along the hill slope is considerably slower than that in the proximal, flatter portion of the line, but because of the well-known problems of surface-wave analysis in topographically complex regions (e.g., Luo *et al.*, 2009) or sloping interfaces (Kuo and Thompson, 1963), we sought independent confirmation of this apparent thickening of slow-velocity material. Larmat *et al.* (2012) came to a similar conclusion through modeling the *Rg* attenuations along this profile; fitting the observed amplitudes required a thicker column of slow, shallow material where the slope begins to steepen.

Efforts to characterize the seismic velocities on other geophone lines have proven challenging. Line 4, which runs to the southwest from the shot and crosses the Boundary fault (Fig. 1), then transverses complex topography, is not possible to constrain well with the current, single-source data. First-arriving *P*-wave times are presented in Figure 11, illustrating the problem from a body-wave perspective. Figure 16 shows the time-domain *Rg* phase velocities, which we can attempt to interpret with a theoretical *Rg* dispersion curve, but the scatter in the data for the stations whose phases appear to exhibit some coherency (ch8–ch14,

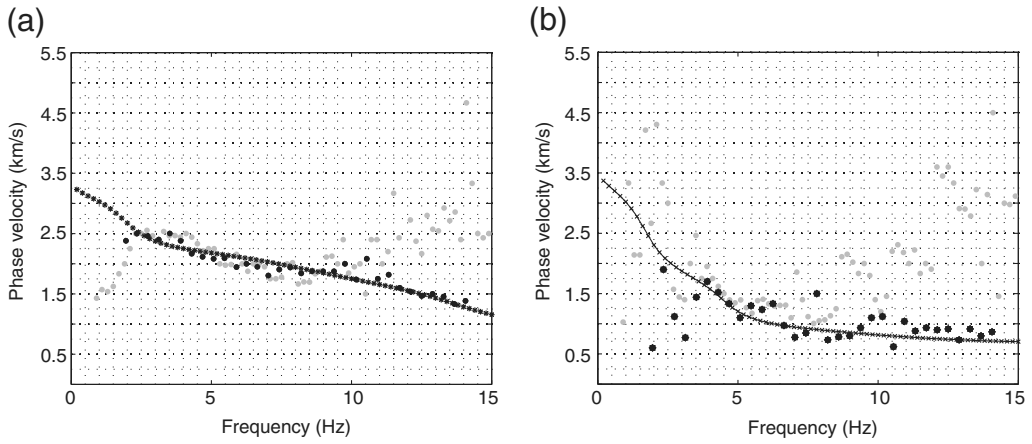

Figure 14. Theoretical *Rg* curves predicted for (a) proximal and (b) distal segments of line 1, based on body-wave models presented in Table 4. Gray circles, time-domain measurements; black circles, frequency-domain measurements; asterisks and crosses, predicted dispersion curves.

Table 4
Final Models for Line 1

Proximal Depth to Interface (m)	V_P Proximal	V_S Proximal	Distal Depth to Interface (m)	V_P Distal	V_S Distal
2	1.0	0.58	5	0.95	0.55
10	1.35	0.78	30	1.35	0.578
30	1.8	1.04	100	2.0	1.16
480	4.5	2.60	550	4.5	2.60
Inf	6.2	3.58	Inf	6.6	3.76

1D body-wave models for proximal and distal segments of line 1. We used a constant V_P/V_S of 1.73 in the modeling with values of density consistent with values derived from well logs (Townsend and Mercadante, 2014).

800–1400 m from the shot), is significant, and the fit is poor. We attribute this to the shallow structural complexities which interfere with the coherent propagation of surface waves at these frequencies (e.g., Stokoe *et al.*, 1994; Ganji *et al.*, 1998). Lines 3 and 5 are even more challenging and are not included in the current analysis.

Conclusions

Research underway through the SPE is intended to better model details of seismic-wave generation (along with other phenomena) from explosion sources at different burial depths. This work, which seeks to advance our ability to characterize explosion sources and the resulting distant seismic observations for the nuclear monitoring community, relies upon modeling of experimental observations in the presence of a known seismic velocity structure. We present here initial efforts in support of the SPE source modelers, to determine the seismic-velocity structure along five geophone lines that extend radially from the SPE source borehole. The anticipated simplicity of the experimental site is shown by our body wave and *Rg* phase dispersion modeling to be complex, and the experimental design inadequate for a robust seismic velocity characterization of the site. We have, however, been able to demonstrate qualitative agreement between body-wave and surface-wave analyses, which provide the initial crude models on which more detailed analyses can be built.

New data from additional planned seismic sources will allow us to illuminate the highly variable, shallow horizons in much greater detail, which is important for modeling the near-source effects such as crushing, spall, slap-down, and other higher-order geologic responses to large explosion detonations at depth.

Data and Resources

Much of the data analysis was performed using the Seismic Analysis Code (SAC). The waveform data used in this analysis were obtained via the Source Physics Experiments (SPE) project and have been archived at the Incorporated Research Institutions for Seismology Data Management Center. Waveforms can be found for SPE-1 (http://www.iris.edu/data/reports/2014/14-017), (http://ds.iris.edu/data/reports/2014/14-067) and SPE-3 (http://ds.iris.edu/data/reports/2014/14-068) in the assembled data sets. Reports were last accessed on July 2015. Full explanations of the data acquisition and processing are provided in Townsend and Mercadente (2014) and Townsend and Obi (2014). MATLAB is available from www.mathworks.com/products/matlab.

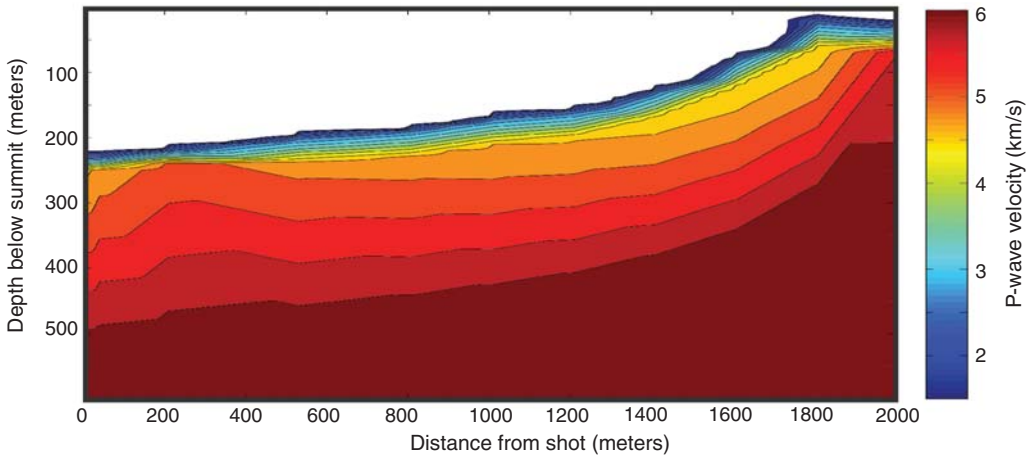

Figure 15. Velocity contours obtained through application of the RAYINVR (Zelt and Smith, 1992) 2D ray-tracing program to *P*-wave arrivals on line 1. Layer horizons were held fixed, but velocities allowed to vary, to reduce predicted arrival misfit compared with observations. Reduction in misfit was 45% compared with homogeneous strata.

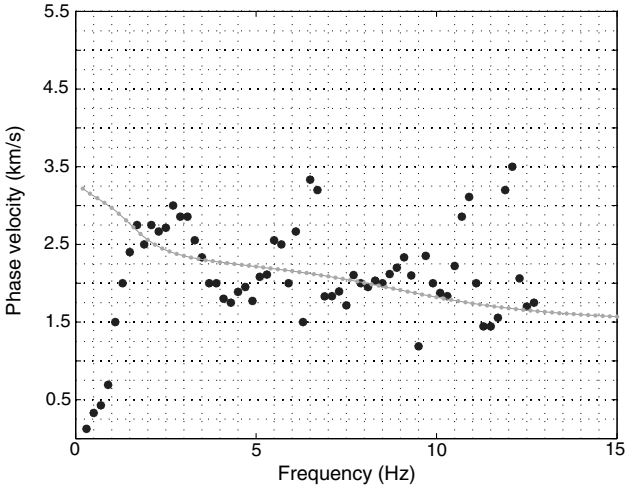

Figure 16. *Rg* phase velocity measurements (black circles) for line 4 stations beyond the Boundary fault. A predicted theoretical curve is shown (gray markers) but the fit is poor and our analysis method given the currently available data does not appear viable for this line.

Acknowledgments

The Source Physics Experiments (SPE) would not have been possible without the support of many people from several organizations. We thank Jonathan MacCarthy for constructive review comments. The authors wish to express their gratitude to the National Nuclear Security Administration, Defense Nuclear Nonproliferation Research and Development (DNN R&D), and the SPE working group, a multi-institutional and interdisciplinary group of scientists and engineers. This work was performed at Los Alamos National Laboratory under Award Number DE-AC52-06NA25946. This is Los Alamos Unlimited Release Number LA-UR-14-28128. Some data analysis and display were performed using Seismic Analysis Code (SAC) (Goldstein *et al.*, 2003) and MATLAB (see Data and Resources).

References

Al-Hunaidi, M. O. (1992). Difficulties with phase spectrum unwrapping in spectral analysis of surface waves nondestructive testing of pavements, *Can. Geotech. J.* **29,** 506–511.

Astrom, K., and K.-E. Lund (1994). Thin superficial layer and lateral heterogeneities in southern Sweden using short-period Rayleigh wave dispersion, *Geophys. J. Int.* **118,** 231–244.

Dobrin, M. B. (1952). *Introduction to Geophysical Prospecting*, McGraw Hill, New York, 435 pp.

Ganji, V., N. Gucunski, and S. Nazarian (1998). Automated inversion procedure for spectral analysis of surface waves, *J. Geotech. Eng. ASCE* **124,** 757–770.

Goldstein, P., D. Dodge, M. Firpo, and L. Minner (2003). SAC2000: Signal processing and analysis tools for seismologists and engineers, invited contribution to *The IASPEI International Handbook of Earthquake and Engineering Seismology*, W. H. K. Lee, H. Kanamori, P. C. Jennings, and C. Kisslinger (Editors), Academic Press, London, United Kingdom.

Heisey, J. S., K. H. Stokoe, and A. H. Meyer (1982). Moduli of pavement systems from spectral analysis of surface waves, *Transportation Research Record 852*, Transportation Research Board, Washington, D.C., 22–31.

Julià, J., C. J. Ammon, R. B. Herrmann, and A. M. Correig (2000). Joint inversion of receiver function and surface wave dispersion observations, *Geophys. J. Int.* **143,** 99–112.

Kuo, J. T., and G. A. Thompson (1963). Model studies on the effect of a sloping interface on Rayleigh waves, *J. Geophys. Res.* **68,** 6187–6197.

Larmat, C. S., C. A. Rowe, and H. J. Patton (2012). Structure modeling and validation applied to Source Physics Experiments (SPEs), presented at *2012 Fall Meeting, AGU*, San Francisco, California, 3–7 December, Abstract S21C-06.

Lawrence, J. F., and D. A. Wiens (2004). Combined receiver-function and surface wave phase-velocity inversion using a Niching genetic algorithm: Application to Patagonia, *Bull. Seismol. Soc. Am.* **94,** 977–987, doi: 10.1785/0120030172.

Luo, Y., X. Jianghai, X. Yixian, Z. Chong, R. D. Miller, and Q. Liu (2009). Dipping-interface mapping using mode-separated Rayleigh waves, *Pure Appl. Geophys.* **166,** 353–374.

Mellors, R. J., S. Myers, S. Ford, W. R. Walter, T. Hauk, S. Ruppert, and A. Pitarka (2012). SPE-3 Far-field Quicklook, *Lawrence Livermore National Laboratory Report LLNL-TR-586676*, 17 pp.

Park, C. B., R. D. Miller, and J. Xia (1999). Multichannel analysis of surface waves, Kansas Geological Survey, *Geophysics* **64,** 800–808.

Rodgers, A. J., N. A. Petersson, and B. Sjogreen (2010). Simulation of topographic effects on seismic waves from shallow explosions near the North Korean nuclear test site with emphasis on shear wave generation, *J. Geophys. Res.* **115,** no. B11309, 27, doi: 10.1029/2010JB007707.

Ryden, N. (2004). Surface wave testing of pavements, *Doctoral Thesis*, Dept. of Engineering Geology, Lund Institute of Technology, Lund University, Sweden, 139 pp.

Schwab, F., K. Nakanishi, M. Cuscito, G. F. Panza, G. Liang, and J. Frez (1984). Surface-wave computations and the synthesis of theoretical seismograms at high frequencies, *Bull. Seismol. Soc. Am.* **74,** 1555–1578.

Snelson, C. M., R. E. Abbott, S. T. Broome, H. J. Patton, A. J. Sussman, M. J. Townsend, and W. R. Walter (2013). Chemical explosion experiments to improve nuclear test monitoring, *Eos Trans. AGU* **94,** 237–239.

Stokoe, K. H., II, S. G. Wright, J. A. Bay, and J. M. Roesset (1994). Characterization of geotechnical sites by SASW method, in *Geophysical Characterization of Sites, ISSMFE Technical Committee Number 10*, R. D. Woods (Editor), Oxford Publishers, New Delhi.

Townsend, M., and J. Mercadante (2014). Data release report for Source Physics Experiment 1 (SPE-1), Nevada National Security Site, *National Security Technologies Technical Report DOE/NV/25946–2018*, 197 pp.

Townsend, M., and C. Obi (2014). Data release report for Source Physics Experiments 2 and 3 (SPE-2 and SPE-3), Nevada national Security Site, *National Security Technologies Technical Report DOE/NV/25946-2282*, 225 pp.

Townsend, M., L. B. Prothero, and C. Obi (2012). Geology of the Source Physics Experiment Site, Climax Stock, Nevada National Security Site, *National Security Technologies Report DOE/NV/25946–1448*, 707 pp.

Zelt, C. A., and R. B. Smith (1992). Seismic traveltime inversion for 2-D crustal velocity structure, *Geophys. J. Int.* **108,** 16–34.

Los Alamos National Laboratory
EES-17, M.S. F-665
Los Alamos, New Mexico 87545
char@lanl.gov

Manuscript received 20 January 2015;
Published Online 1 September 2015